Electronic Supplementary Information for

Synergetic stability enhancement with magnesium and calcium ion substitution for Ni/Mn-based P2-type sodium-ion battery cathodes

Hongwei Fu,‡[a] Yun-Peng Wang,‡[b] Guozheng Fan,[c] Shan Guo,[a] Xuesong Xie,[a] Xinxin Cao,[a] Bingan Lu,[d] Mengqiu Long,[e] Jiang Zhou*[af] and Shuquan Liang*[a]

[a] School of Materials Science and Engineering, Key Laboratory of Electronic Packaging and Advanced Functional Materials of Hunan Province, Central South University, Changsha 410083, China.

[b] School of Physics and Electronics, Hunan Key Laboratory for Super-micro structure and Ultrafast Process, Central South University, 932 South Lushan Road, Changsha, China.

[c] Bremen Center for Computational Materials Science, University of Bremen, Bremen 28359, Germany.

[d] School of Physics and Electronics, State Key Laboratory of Advanced Design and Manufacturing for Vehicle Body, Hunan University, Changsha 410082, China.

[e] School of Physics and Electronics, Central South University, Changsha 410083, Hunan, P.R. China.

[f] College of Chemistry and Chemical Engineering, Jishou University, Jishou, Hunan 416000, P. R. China.

* Corresponding authors.

E-mail: zhou_jiang@csu.edu.cn; lsq@csu.edu.cn

‡ These authors contributed equally to this work.

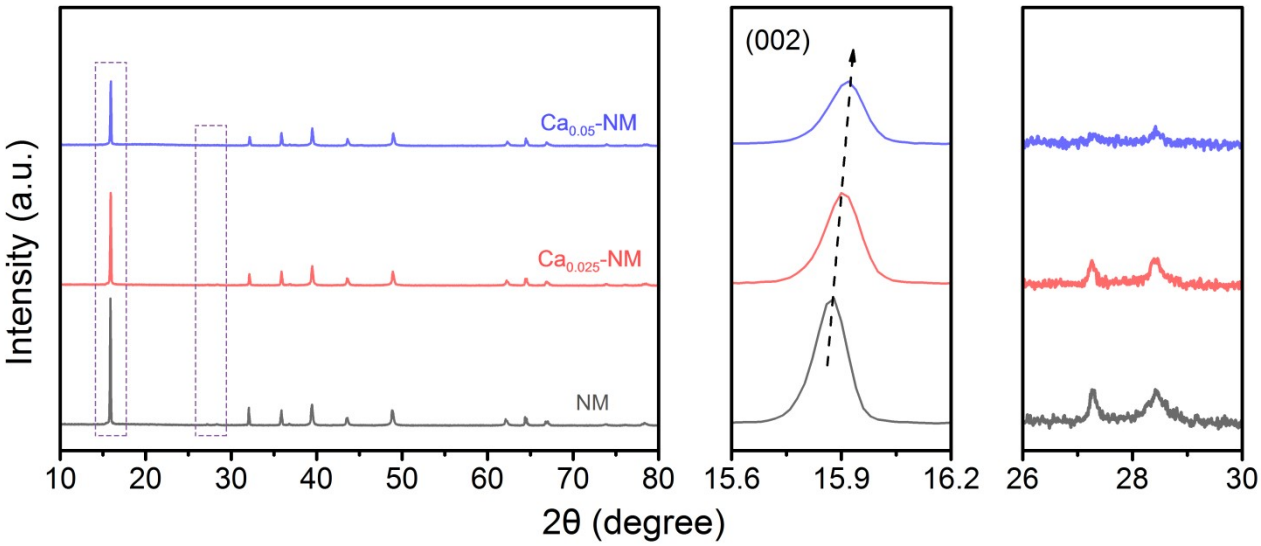

Fig. S1 The XRD patterns of NM, $Ca_{0.025}$-NM and $Ca_{0.05}$-NM.

The introduction of Ca^{2+} ions into the alkali-metal layers causing the (002) peak to shift to higher angle, indicating the shrinkage of parameter '*c*'. Moreover, Na^{+} ions ordering is also suppressed with Ca^{2+} ions, as the superlattice peaks between 26–30° are weakened.

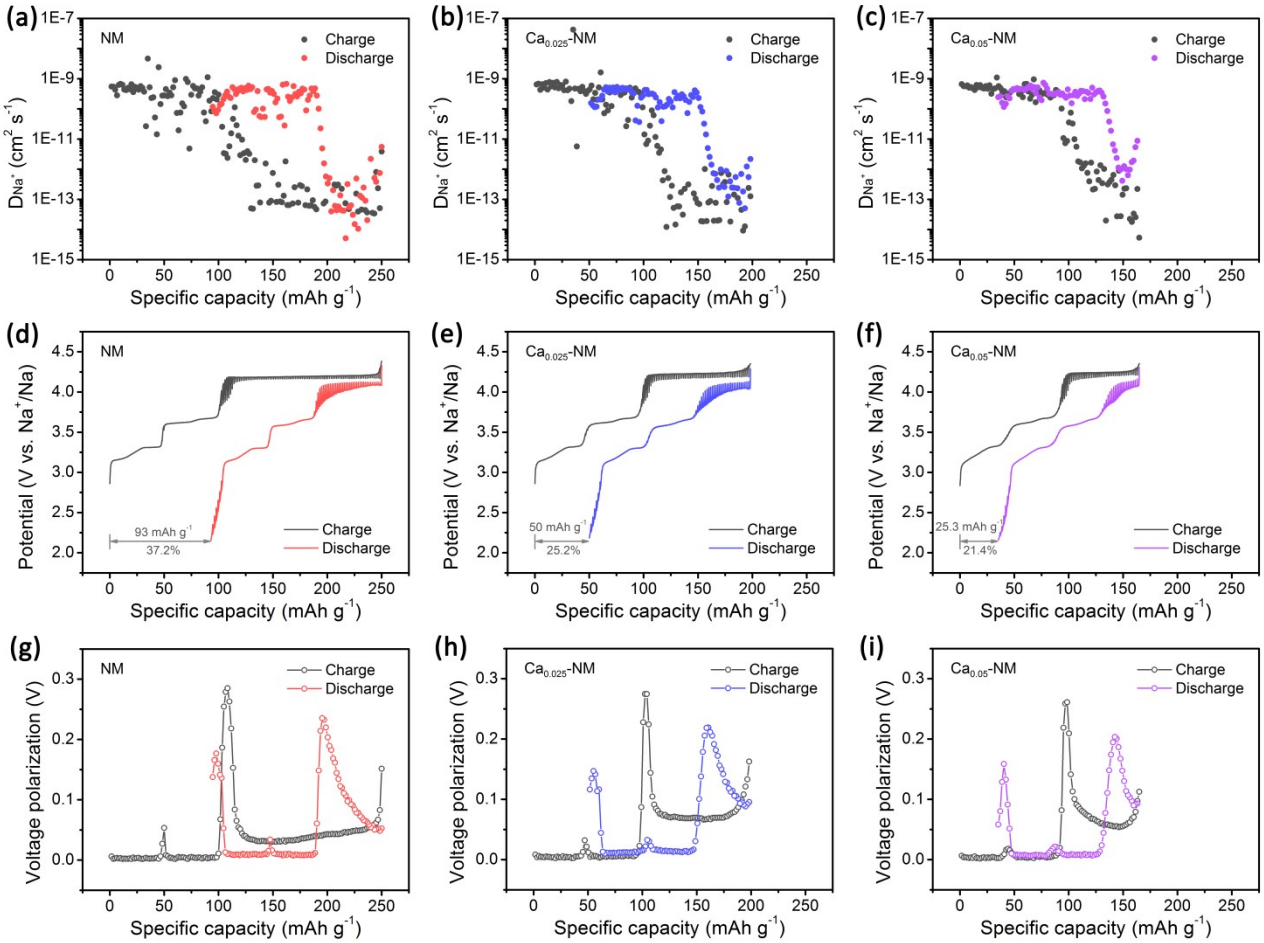

Fig. S2 The Na^+ diffusion coefficient of (a) NM, (b) $Ca_{0.025}$-NM and (c) $Ca_{0.05}$-NM. The 1st cycle GITT curves of (d) NM, (e) $Ca_{0.025}$-NM and (f) $Ca_{0.05}$-NM. Corresponding voltage polarization of (g) NM, (h) $Ca_{0.025}$-NM and (i) $Ca_{0.05}$-NM.

Although the suppressing of P2-O2 phase transition improve the Na^+ diffusion coefficient at the 4.2 V plateau region with Ca^{2+} pillars, the voltage polarization here raises. This infers the deterioration of the kinetics involving high-voltage reactions.

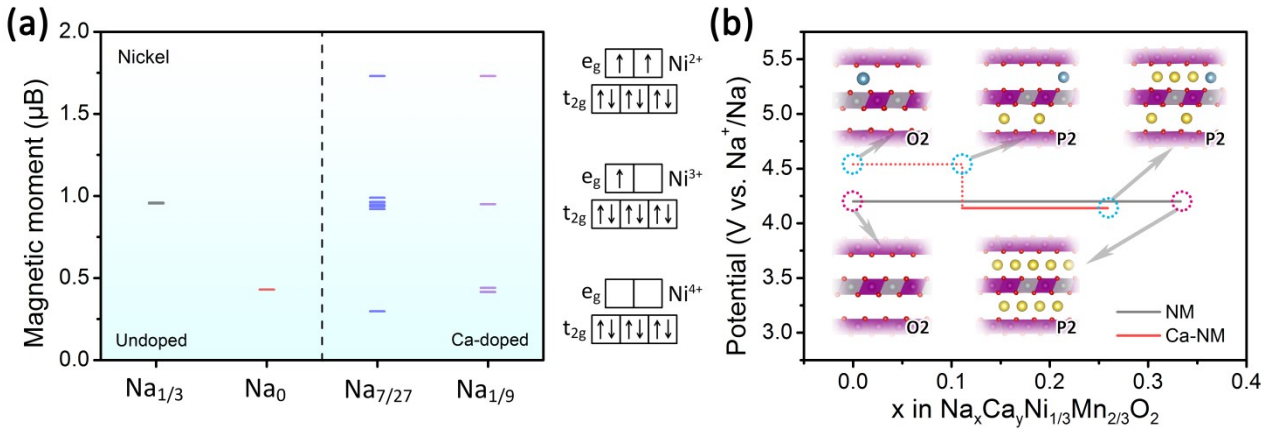

Fig. S3 (a) The magnetic moment for Ni of NM at Na = 1/3 and 0, and Ca-NM at Na = 7/27 and 1/9, respectively. (b) The calculated redox potential for NM and Ca-NM with positive charge less than 1/3 in AM layers.

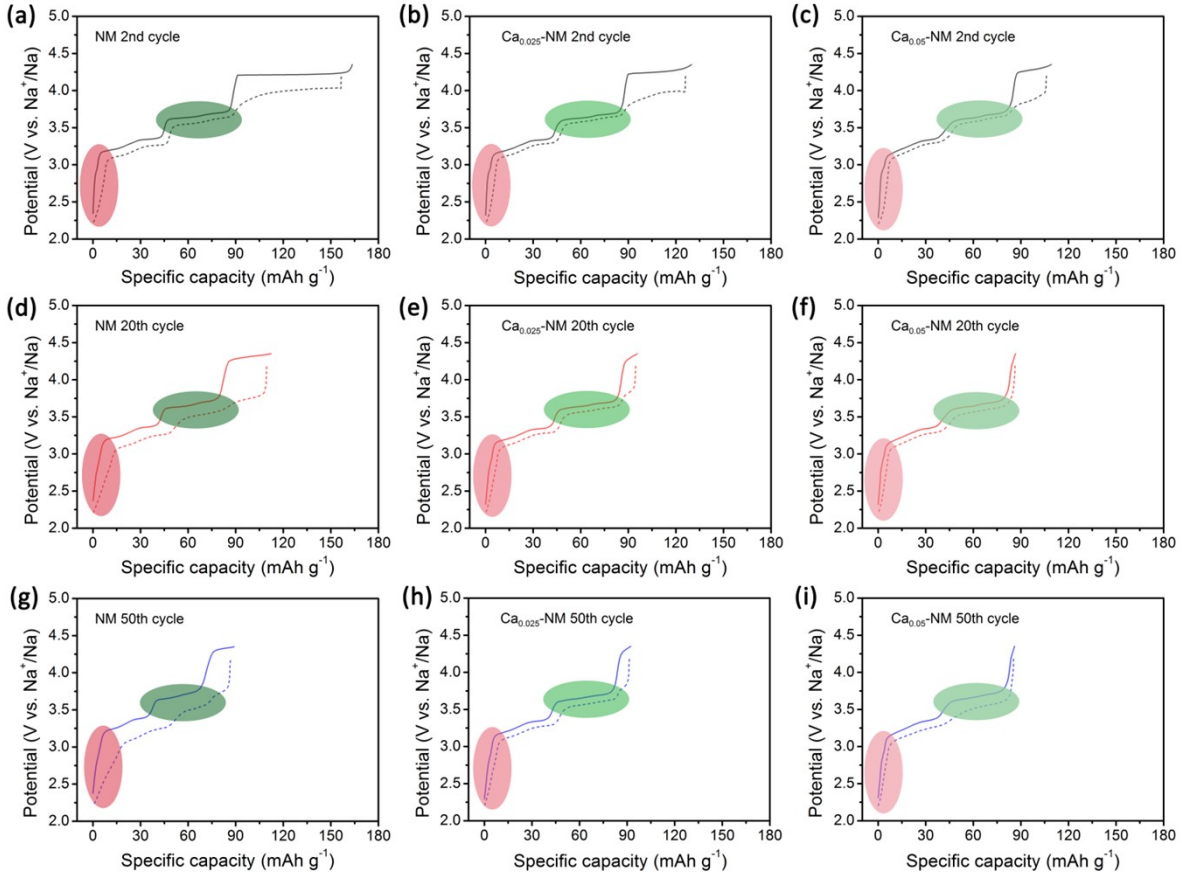

Fig. S4 The charge-discharge profiles of the 2nd cycle of (a) NM, (b) $Ca_{0.025}$-NM and (c) $Ca_{0.05}$-NM. The charge-discharge profiles of the 20th cycle of (d) NM, (e) $Ca_{0.025}$-NM and (f) $Ca_{0.05}$-NM. The charge-discharge profiles of the 50th cycle of (g) NM, (h) $Ca_{0.025}$-NM and (i) $Ca_{0.05}$-NM.

The two plateaus below 4.1 V have similar overpotential at the 2nd cycle for NM, meaning the identical redox here. When cycling continues, the charge and the discharge capacities at the 3.6 V plateau become unequal. Relatively, the discharge capacity at the 2.2–3 V slope region obviously surpasses the corresponding charge capacity. And this abnormal high overpotential is unlikely to be resulted from the deterioration of Na^+ diffusion or continuous electrolyte decomposition, since they will cause global overpotential increment. Given that the migration of TM ions can increase the voltage hysteresis of the oxygen redox, as the superstructure loses,[1, 2] some capacity below 4.1 V might also be affected, since the oxygen redox exists below 4.1 V in the NM.[3]

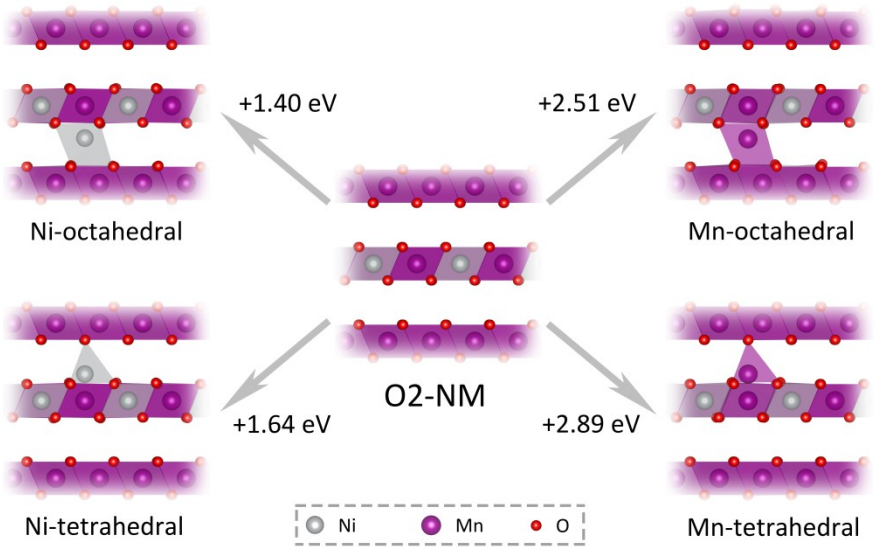

Fig. S5 The energy difference between O2-$Na_0Ni_{1/3}Mn_{2/3}O_2$ and its derivatives with TM migration.

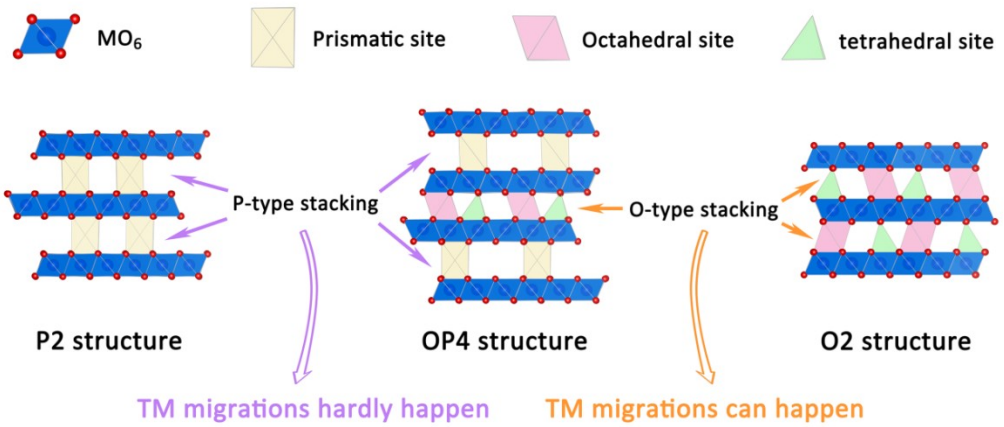

Fig. S6 Schematic illustrations of P2, OP4 and O2 structures. Three types of site in the AM layers are presented.

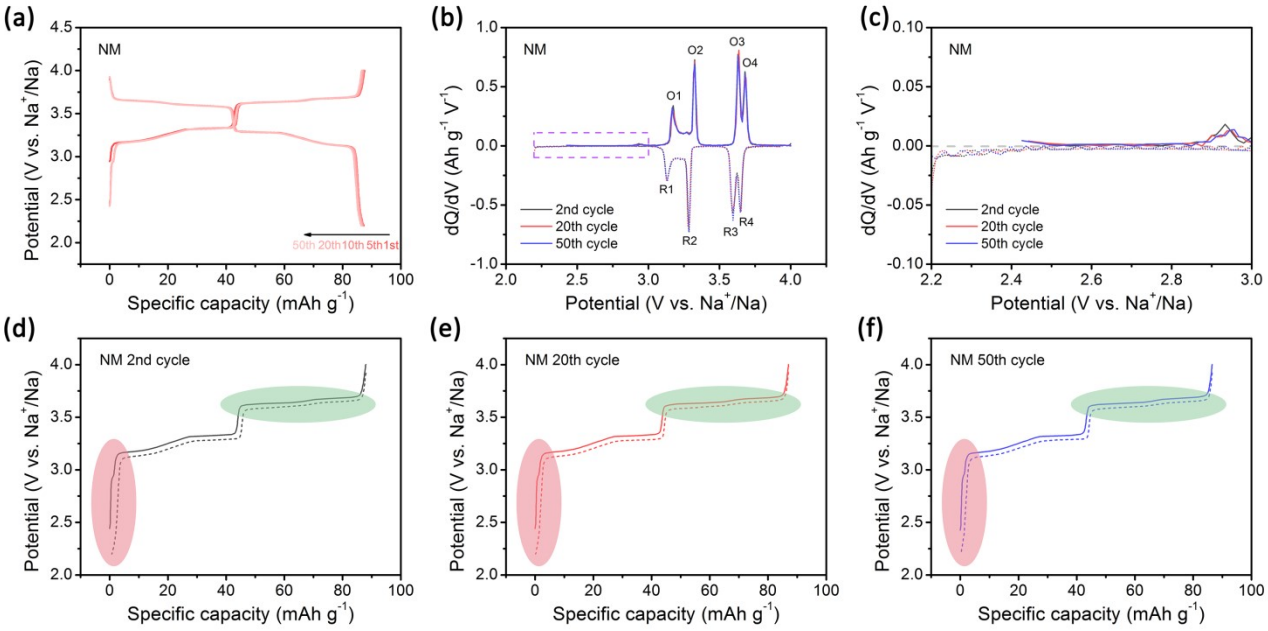

Fig. S7 (a) The charge-discharge profiles at 50 mA g^{-1} of NM. (b) The dQ/dV plots of NM. (c) Enlarged views of dQ/dV plots between 2.2 and 3 V of NM. The charge-discharge profiles of NM at (d) the 2nd cycle, (e) the 20th cycle and (f) the 50th cycle.

When NM cycles in the voltage range of 2.2–4 V, the charge-discharge profiles are almost unchanged, keeping good symmetry. No capacity with abnormal high overpotential appears, no significant variation of the redox peaks is observed, inferring that the structure is maintained well with the avoidance of P2-O2 phase transition.

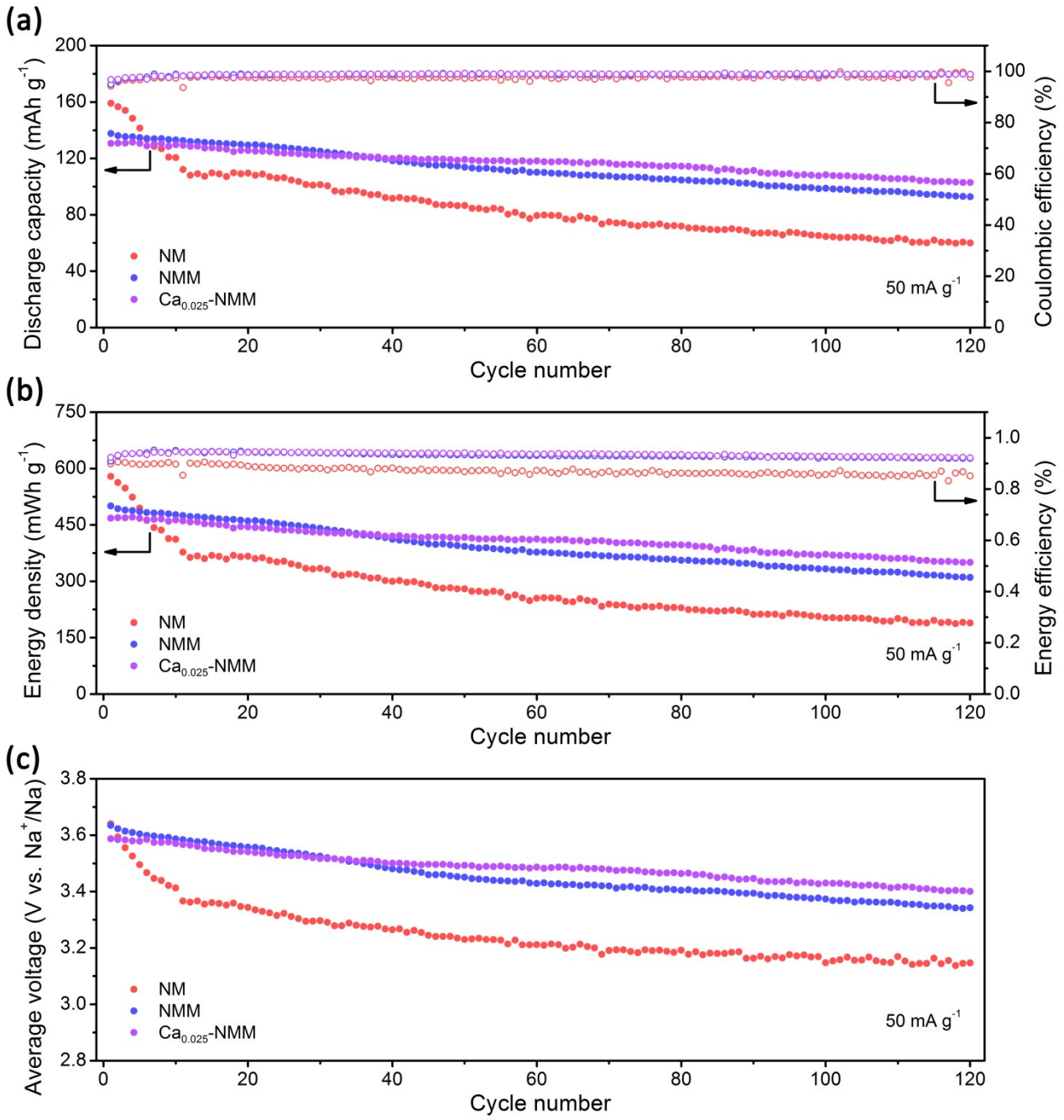

Fig. S8 Comparison of (a) the cycling capacity and coulombic efficiency, (b) discharge energy density and energy efficiency and (c) average discharge voltage of NM, NMM and $Ca_{0.025}$-NMM.

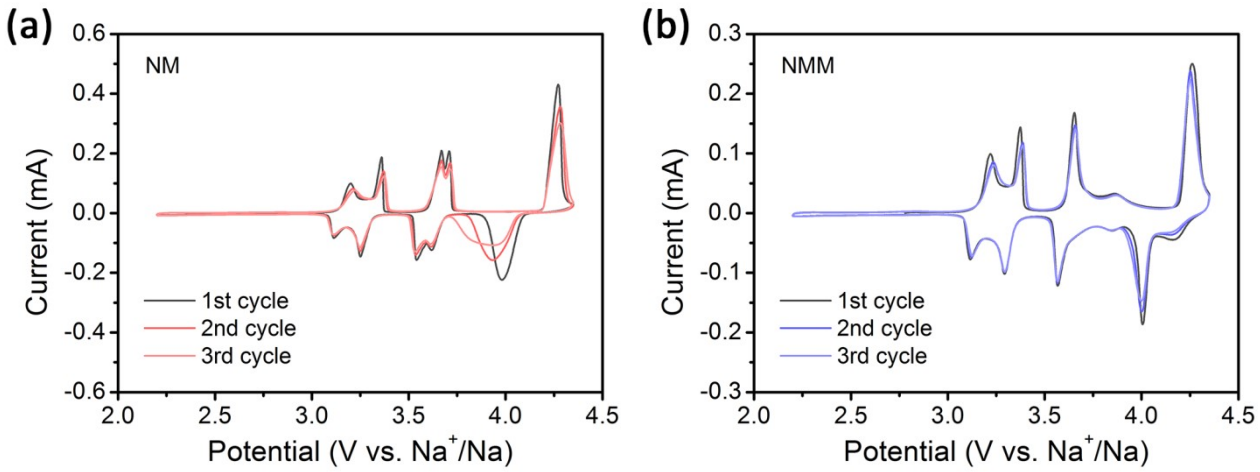

Fig. S9 CV curves of (a) NM and (b) NMM.

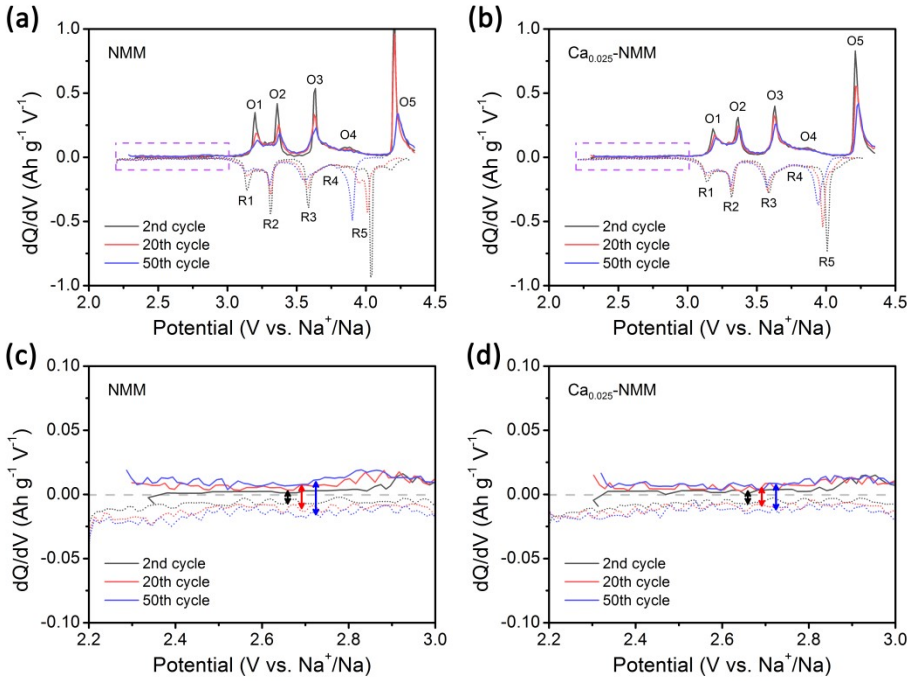

Fig. S10 The dQ/dV plots of (a) NMM and (b) $Ca_{0.025}$-NMM. Enlarged views of dQ/dV plots between 2.2 and 3 V of (c) NMM and (d) $Ca_{0.025}$-NMM.

Unlike NM, the symmetry at the 2.2–3 V slope region maintains well for Mg-doped samples upon cycling, with an increasing capacity at both charge and discharge processes. Therefore, the change here should not be ascribed to TM ions migration. Commonly, Mn^{4+}/Mn^{3+} redox mainly occurs below 2 V for $Na_{2/3}Ni_{1/3}Mn_{2/3}O_2$.[4, 5]

While for Mn-based materials without using nickel, Mn^{4+}/Mn^{3+} redox can take place at higher voltage.[6-11] Given that Mg^{2+} can migrate from the TM layers to the AM layers and further aggregate, from the publication of Sui and co-workers,[12] we suppose that micro-regions with high manganese content will form during high-cut-off voltage cycling, and further trigger the reactivity of Mn^{4+}/Mn^{3+} redox.

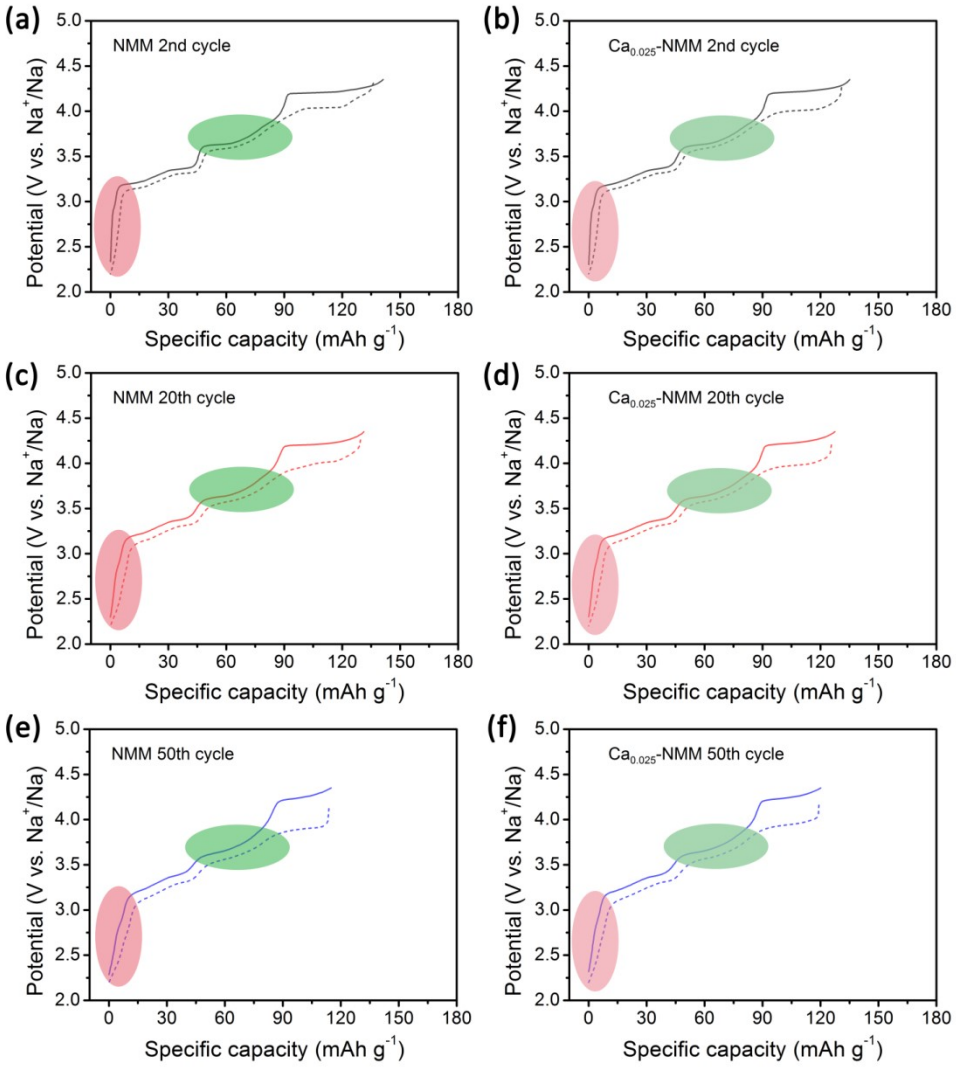

Fig. S11 The charge-discharge profiles of the 2nd cycle of (a) NMM and (b) $Ca_{0.025}$-NMM. The charge-discharge profiles of the 20th cycle of (c) NMM and (d) $Ca_{0.025}$-NMM. The charge-discharge profiles of the 50th cycle of (e) NMM and (f) $Ca_{0.025}$-NMM.

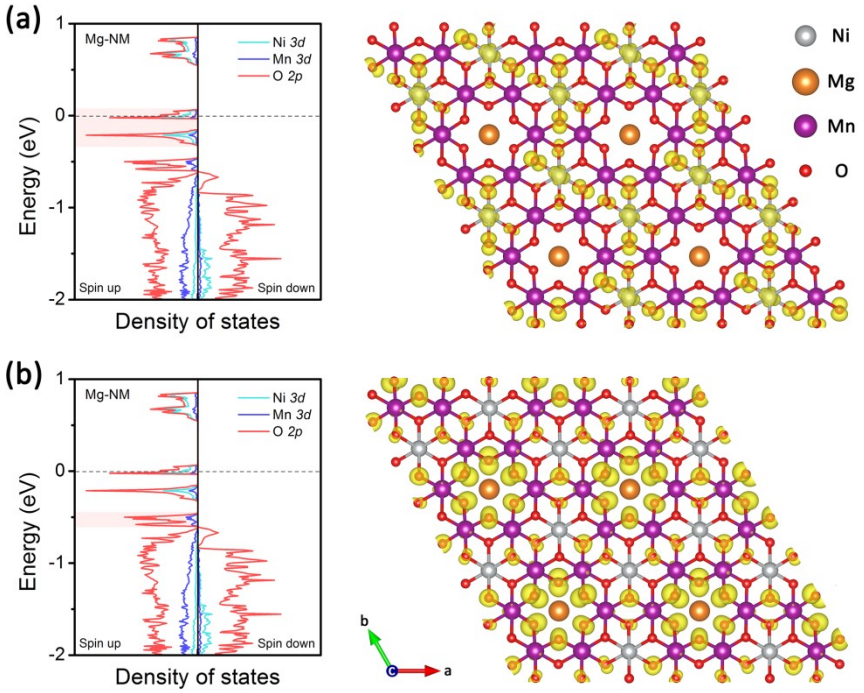

Fig. S12 (a) The spatial charge density at -0.31 < E-E_F < 0.06 eV, and (b) at -0.6 < E-E_F < -0.45 eV of Mg-NM at Na content of 1/3.

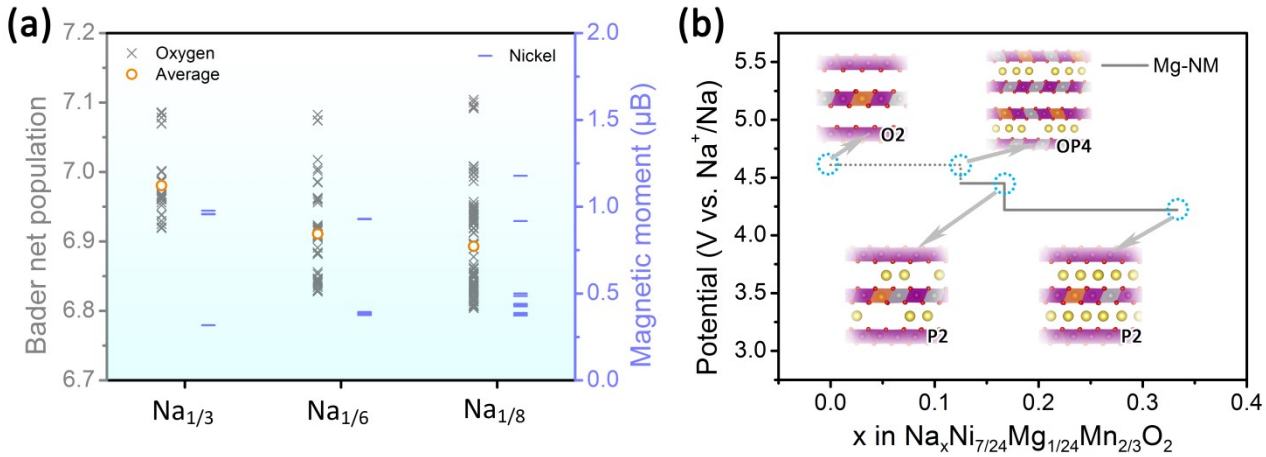

Fig. S13 (a) The Bader charge for O and the magnetic moment for Ni of Mg-NM at Na = 1/3, 1/6 and 1/8, respectively. (b) The calculated redox potential for Mg-NM with positive charge less than 1/3 in AM layers.

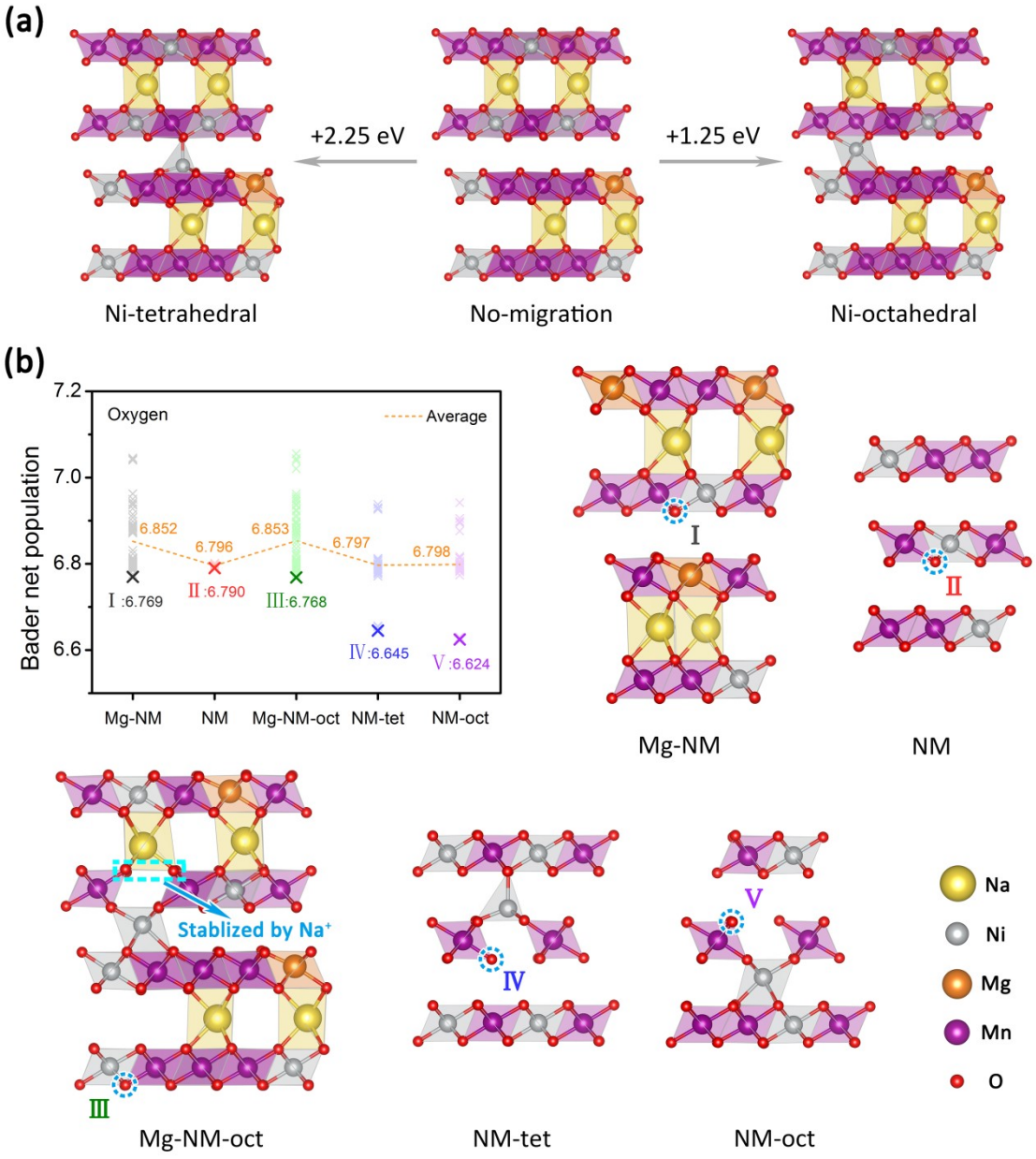

Fig. S14 (a) The energy difference between OP4-Mg-NM (Na = 1/9) and its derivatives with TM migration. (b) The Bader charge for O of OP4-Mg-NM (Na = 1/9), OP4-Mg-NM (Na = 1/9) with one Ni ion in octahedral site, O2-NM (Na = 0), O2-NM (Na = 0) with one Ni ion in tetrahedral site and O2-NM (Na = 0) with one Ni ion in octahedral site, respectively. And corresponding relaxed structures with labeled O atom with the smallest Bader charge.

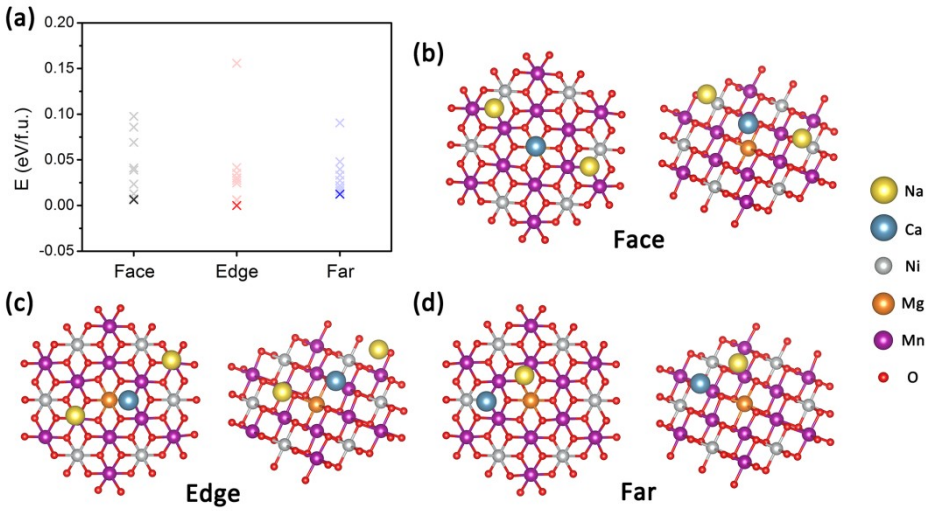

Fig. S15 (a) The energetics of possible configurations of structures for $Na_{4/18}Ca_{1/18}Ni_{5/18}Mg_{1/18}Mn_{12/18}O_2$. (b) The optimized structure with Ca in the face-shared site near Mg. (c) The optimized structure with Ca in the edge-shared site near Mg. (d) The optimized structure with Ca away from Mg.

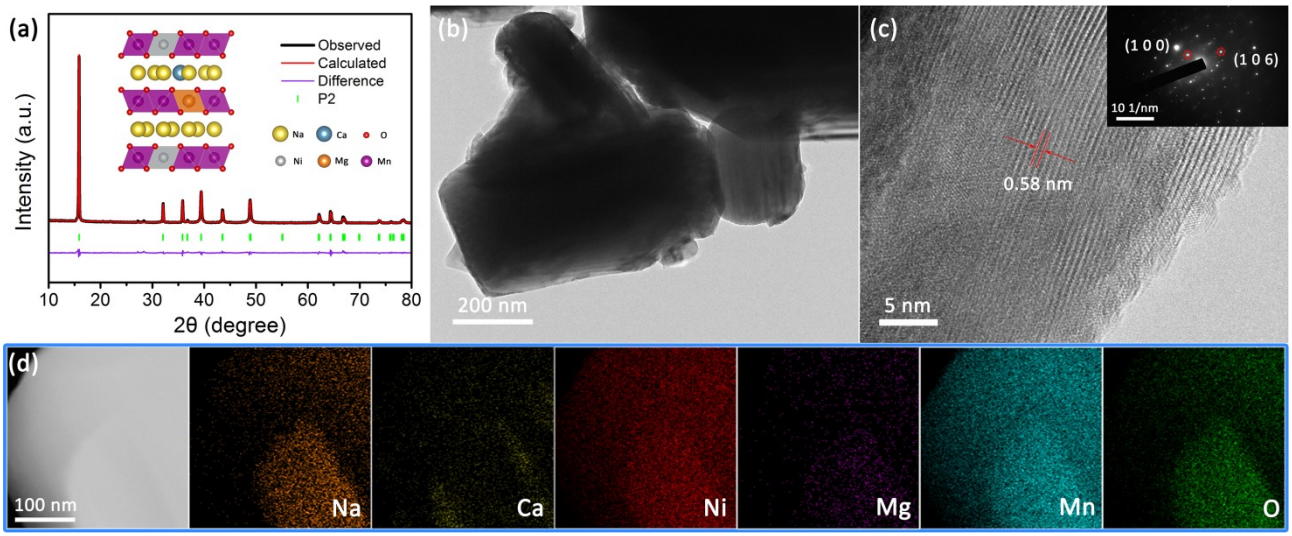

Fig. S16 (a) The XRD pattern and Rietveld refinement, (b) TEM image, (c) HRTEM image (inset shows corresponding selected area electron diffraction pattern) and (d) EDS maps of $Ca_{0.025}$-NMM.

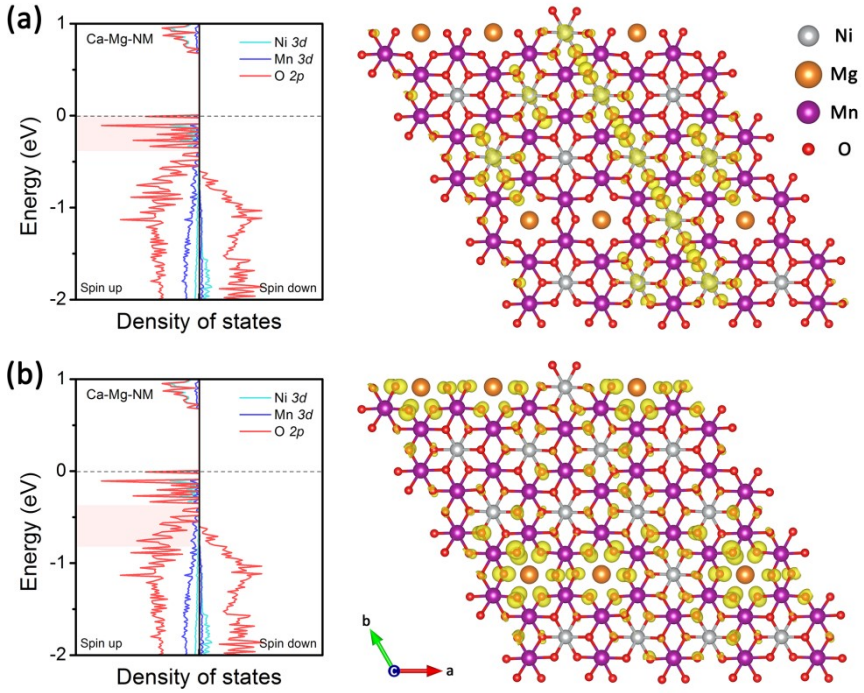

Fig. S17 (a) The spatial charge density at -0.37 < E-E_F < 0.00 eV, and (b) at -0.82 < E-E_F < -0.37 eV of Ca-Mg-NM at Na content of 7/27.

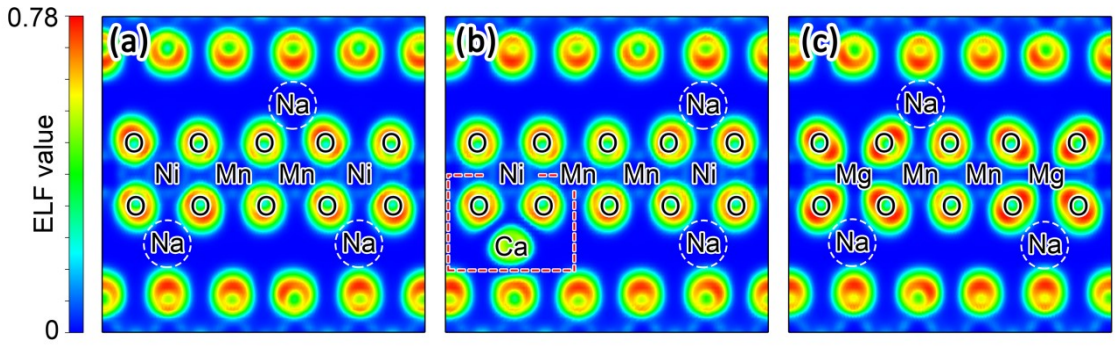

Fig. S18 The ELF maps of (a) NM, (b) Ca-NM and (c) Mg-NM (visualized by VESTA). Ca ions have more significant impact on the electron distribution of the bonding than Na ions.

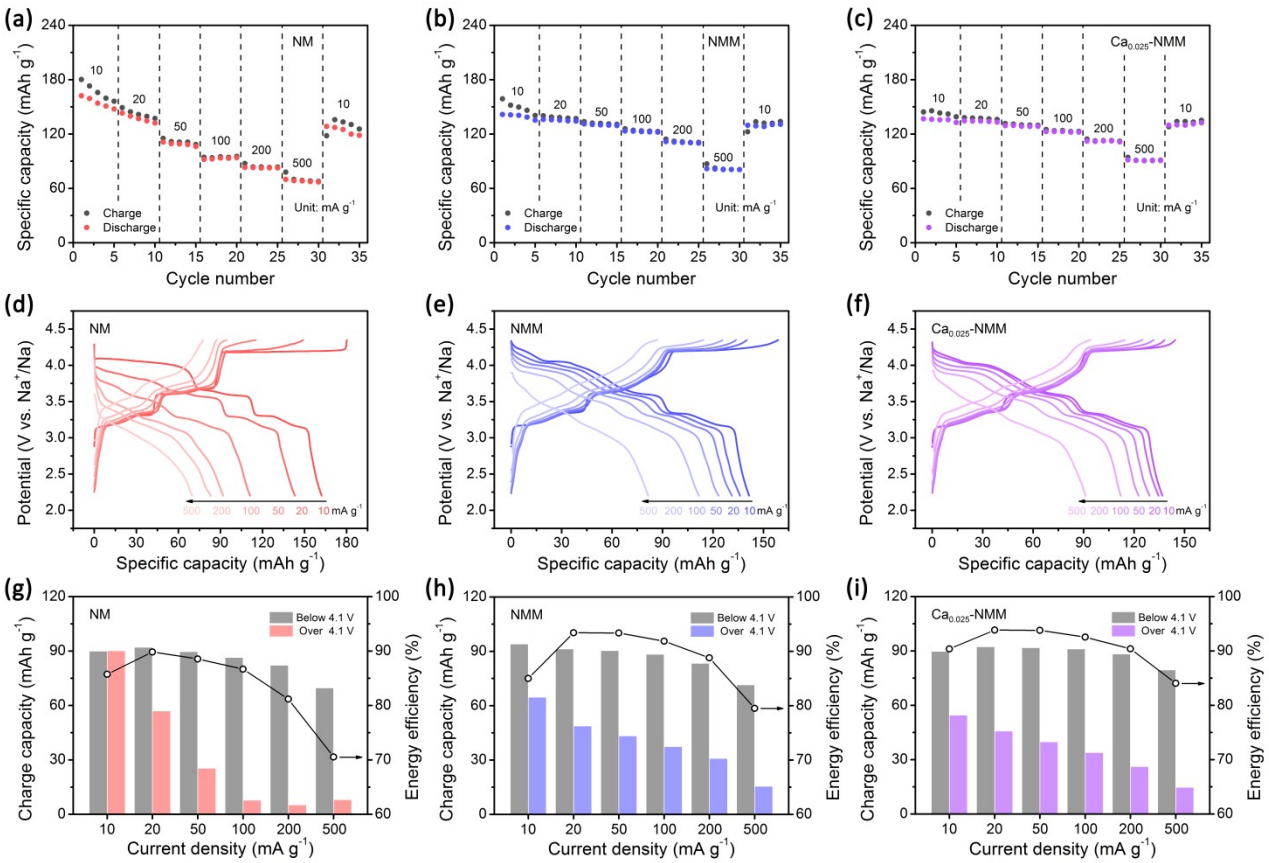

Fig. S19 The rate performance of (a) NM, (b) NMM and (c) $Ca_{0.025}$-NMM. Corresponding charge-discharge profiles of (d) NM, (e) NMM and (f) $Ca_{0.025}$-NMM. Corresponding coulombic efficiency, charge capacity below and over 4.1 V at different current density of (g) NM, (h) NMM and (i) $Ca_{0.025}$-NMM.

We must emphasize that the worst rate performance of NM is not merely coming from the sluggish Na^+ diffusion in the O2 phase. It has been confirmed that NM suffers from serious cracking, electrolyte decomposition, lattice oxygen release and surface densification with high voltage cycling.[12, 13] Therefore, this test of NM undervalues its intrinsic rate performance inevitably.

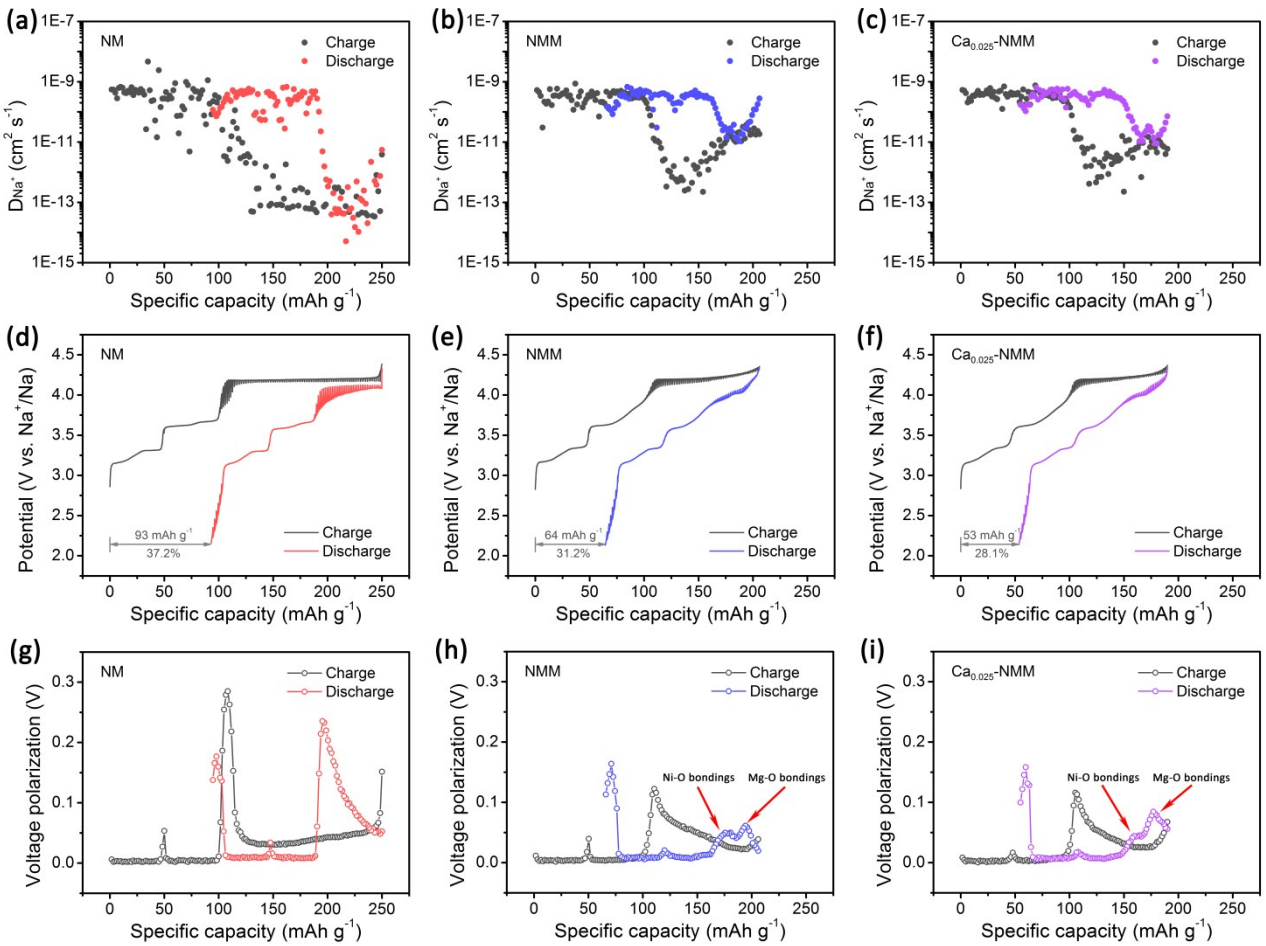

Fig. S20 The Na^+ diffusion coefficient of (a) NM, (b) NMM and (c) $Ca_{0.025}$-NMM. The 1st cycle GITT curves of (d) NM, (e) NMM and (f) $Ca_{0.025}$-NMM. Corresponding voltage polarization of (g) NM, (h) NMM and (i) $Ca_{0.025}$-NMM.

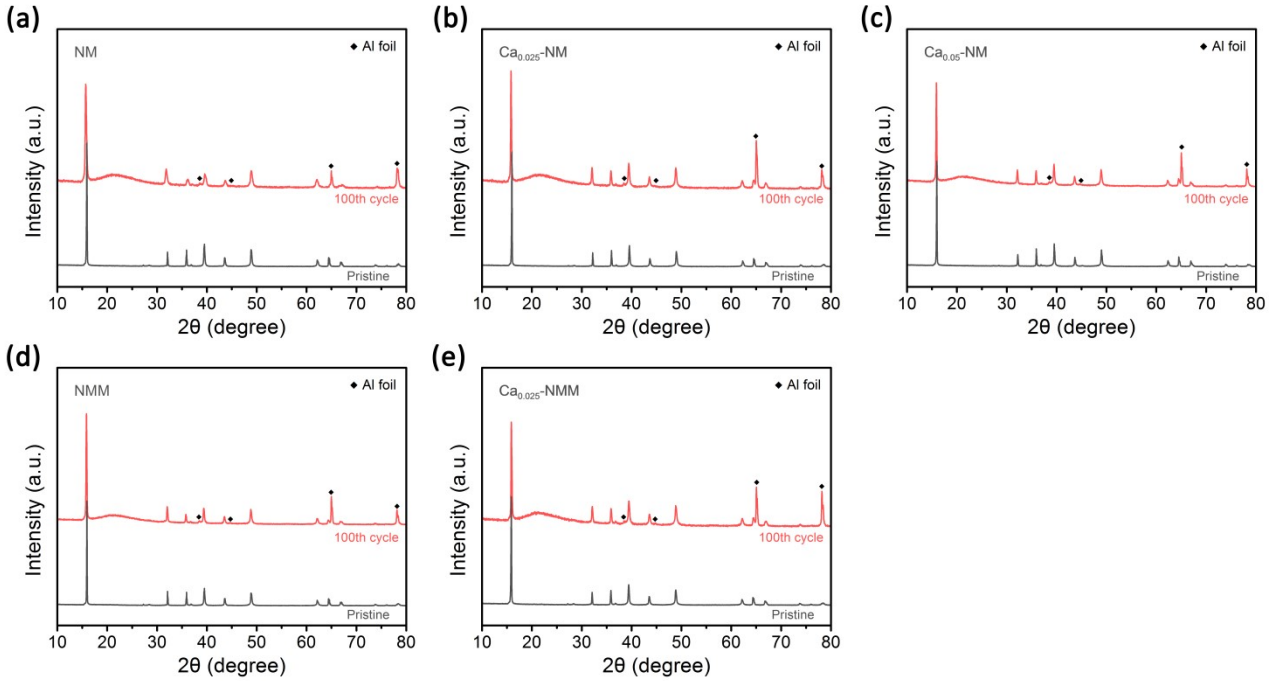

Fig. S21 The XRD pattern comparisons between pristine powder and 100 times cycled electrode of (a) NM, (b) $Ca_{0.025}$-NM, (c) $Ca_{0.05}$-NM, (d) NMM and (e) $Ca_{0.025}$-NMM.

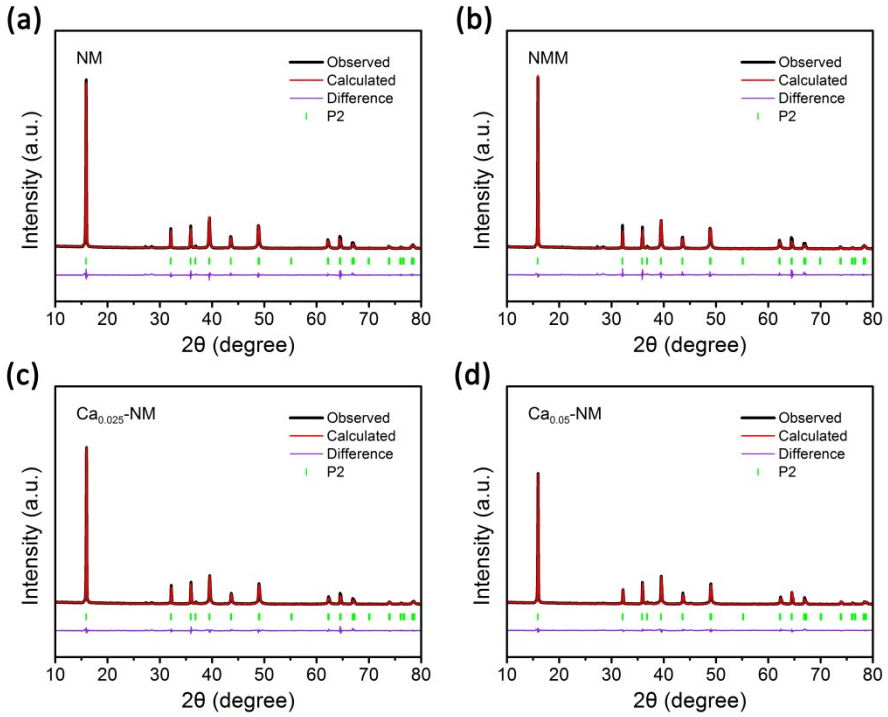

Fig. S22 The Rietveld refinement of XRD patterns of (a) NM, (b) NMM, (c) $Ca_{0.025}$-NM and (d) $Ca_{0.05}$-NM.

Table S1 Crystallographic parameters of NM from Rietveld refinement.

Space Group	*P6₃/mmc* (No. 194)				
Atom	Site	x	y	z	Occ.
Na_f	2b	0.0000	0.0000	0.2500	0.251(3)
Na_e	2d	0.3333	0.6667	0.7500	0.419(3)
Ni	2a	0.0000	0.0000	0.5000	0.330
Mn	2a	0.0000	0.0000	0.5000	0.670
O	4f	0.3333	0.6667	0.0977(4)	1.000
a = 2.89070(7) Å		c = 11.16285(35) Å		V = 80.782(5) Å^3	
R_p = 4.42%		R_{wp} = 6.64%		χ^2 = 2.920	

Table S2 Crystallographic parameters of $Ca_{0.025}$-NM from Rietveld refinement.

Space Group	*P6₃/mmc* (No. 194)				
Atom	Site	x	y	z	Occ.
Na_f	2b	0.0000	0.0000	0.2500	0.224(3)
Na_e	2d	0.3333	0.6667	0.7500	0.396(3)
Ca	2b	0.0000	0.0000	0.2500	0.025
Ni	2a	0.0000	0.0000	0.5000	0.330
Mn	2a	0.0000	0.0000	0.5000	0.670
O	4f	0.3333	0.6667	0.0919(4)	1.000
a = 2.88834(4) Å		c = 11.14400(29) Å		V = 80.513(3) Å^3	
R_p = 4.23%		R_{wp} = 6.05%		χ^2 = 2.286	

Table S3 Crystallographic parameters of $Ca_{0.05}$-NM from Rietveld refinement.

Space Group	*P6₃/mmc* (No. 194)				
Atom	Site	x	y	z	Occ.
Na_f	2b	0.0000	0.0000	0.2500	0.196(2)
Na_e	2d	0.3333	0.6667	0.7500	0.374(2)
Ca	2b	0.0000	0.0000	0.2500	0.050
Ni	2a	0.0000	0.0000	0.5000	0.330
Mn	2a	0.0000	0.0000	0.5000	0.670
O	4f	0.3333	0.6667	0.0895(4)	1.000
a = 2.89118(21) Å		c = 11.14151(88) Å		V = 80.654(16) Å^3	
R_p = 4.17%		R_{wp} = 5.59%		χ^2 = 1.886	

Table S4 Crystallographic parameters of NMM from Rietveld refinement.

Space Group	*P6₃/mmc* (No. 194)				
Atom	Site	x	y	z	Occ.
Na_f	2b	0.0000	0.0000	0.2500	0.261(3)
Na_e	2d	0.3333	0.6667	0.7500	0.409(3)
Ni	2a	0.0000	0.0000	0.5000	0.280
Mg	2a	0.0000	0.0000	0.5000	0.050
Mn	2a	0.0000	0.0000	0.5000	0.670
O	4f	0.3333	0.6667	0.0937(5)	1.000
a = 2.89136(4) Å		c = 11.16626(34) Å		V = 80.843(4) Å^3	
R_p = 4.84%		R_{wp} = 7.42%		χ^2 = 3.290	

Table S5 Crystallographic parameters of $Ca_{0.025}$-NMM from Rietveld refinement.

Space Group	*P6₃/mmc* (No. 194)				
Atom	Site	x	y	z	Occ.
Na_f	2b	0.0000	0.0000	0.2500	0.258(2)
Na_e	2d	0.3333	0.6667	0.7500	0.362(2)
Ca	2b	0.0000	0.0000	0.2500	0.025
Ni	2a	0.0000	0.0000	0.5000	0.280
Mg	2a	0.0000	0.0000	0.5000	0.050
Mn	2a	0.0000	0.0000	0.5000	0.670
O	4f	0.3333	0.6667	0.0931(4)	1.000
a = 2.89081(4) Å		c = 11.15197(32) Å		V = 80.709(3) Å^3	
R_p = 4.28%		R_{wp} = 6.11%		χ^2 = 2.484	

Supplementary References

1 R. A. House, U. Maitra, M. A. Perez-Osorio, J. G. Lozano, L. Jin, J. W. Somerville, L. C. Duda, A. Nag, A. Walters, K. J. Zhou, M. R. Roberts and P. G. Bruce, *Nature*, 2020, **577**, 502-508.

2 R. A. House, G. J. Rees, M. A. Pérez-Osorio, J.-J. Marie, E. Boivin, A. W. Robertson, A. Nag, M. Garcia-Fernandez, K.-J. Zhou and P. G. Bruce, *Nat. Energy*, 2020, **5**, 777-785.

3 K. Dai, J. Mao, Z. Zhuo, Y. Feng, W. Mao, G. Ai, F. Pan, Y.-d. Chuang, G. Liu and W. Yang, *Nano Energy*, 2020, **74**, 104831.

4 Q. Liu, Z. Hu, M. Chen, C. Zou, H. Jin, S. Wang, Q. Gu and S. Chou, *J. Mater. Chem. A*, 2019, **7**, 9215-9221.

5 N. Tapia-Ruiz, W. M. Dose, N. Sharma, H. Chen, J. Heath, J. W. Somerville, U. Maitra, M. S. Islam and P. G. Bruce, *Energy Environ. Sci.*, 2018, **11**, 1470-1479.

6 J. Billaud, G. Singh, A. R. Armstrong, E. Gonzalo, V. Roddatis, M. Armand, T. Rojo and P. G. Bruce, *Energy Environ. Sci.*, 2014, **7**, 1387-1391.

7 R. J. Clément, J. Billaud, A. Robert Armstrong, G. Singh, T. Rojo, P. G. Bruce and C. P. Grey, *Energy Environ. Sci.*, 2016, **9**, 3240-3251.

8 E. de la Llave, E. Talaie, E. Levi, P. K. Nayak, M. Dixit, P. T. Rao, P. Hartmann, F. Chesneau, D. T. Major, M. Greenstein, D. Aurbach and L. F. Nazar, *Chem. of Mater.*, 2016, **28**, 9064-9076.

9 S. Kumakura, Y. Tahara, K. Kubota, K. Chihara and S. Komaba, *Angew. Chem., Int. Ed.*, 2016, **55**, 12760-12763.

10 Y. Li, X. Wang, Y. Gao, Q. Zhang, G. Tan, Q. Kong, S. Bak, G. Lu, X.-Q. Yang, L. Gu, J. Lu, K. Amine, Z. Wang and L. Chen, *Adv. Energy Mater.*, 2019, **9**, 1803087.

11 B. Mortemard de Boisse, S.-i. Nishimura, E. Watanabe, L. Lander, A. Tsuchimoto, J. Kikkawa, E. Kobayashi, D. Asakura, M. Okubo and A. Yamada, *Adv. Energy Mater.*, 2018, **8**, 1800409.

12 K. Wang, H. Wan, P. Yan, X. Chen, J. Fu, Z. Liu, H. Deng, F. Gao and M. Sui, *Adv. Mater.*, 2019, **31**, 1904816.

13 Y. Zhang, M. Wu, J. Ma, G. Wei, Y. Ling, R. Zhang and Y. Huang, *ACS Cent. Sci.*, 2020, **6**, 232-240.